J. Fluid Mech. (2023), *vol*. 970, A38, doi:10.1017/jfm.2023.669

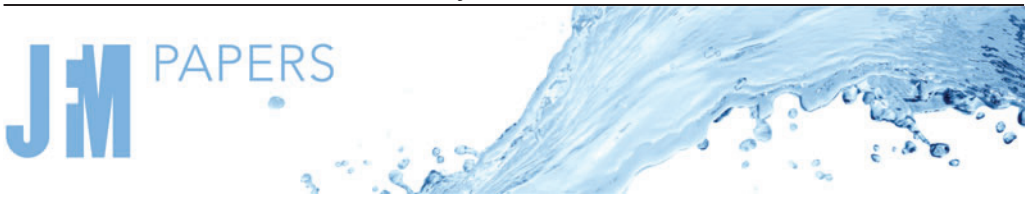

A new probability density function for the surface elevation in irregular seas

David R. Fuhrman[1],†, **Mathias Klahn**[2] **and Yanyan Zhai**[1]

[1]Department of Civil and Mechanical Engineering, Technical University of Denmark, 2800 Kgs. Lyngby, Denmark

[2]Odeon A/S, DTU Science Park, 2800 Kgs. Lyngby, Denmark

(Received 28 March 2023; revised 2 August 2023; accepted 9 August 2023)

To date, the predominant means for computing the probability density function (p.d.f.) for the free surface elevation of a nonlinear, irregular water wave field, free of assumptions involving narrow-bandedness and small directionality, is the approximate Gram–Charlier series solution of Longuet-Higgins (*J. Fluid Mech.*, vol. 17, 1963, pp. 459–480, hereafter LH63). In this paper we re-visit the derivation of this p.d.f. to second order in the wave steepness, utilizing both moment and cumulant generating functions. We show that LH63's approximate solution based on the cumulant generating function, in fact, matches that derived from the moment generating function. Moreover, through a change of variables coupled with complex analysis, it is shown that the approximation employed by LH63 is unnecessary, and the second-order p.d.f. stemming from the cumulant generating function can be represented exactly in terms of the Airy function. The new second-order p.d.f. predicts increased probability of extreme positive surface elevations typical of e.g. rogue waves, relative to both second- and third-order solutions of LH63. This heavy positive tail is inherent, and is explained through comparison of the asymptotic limits of the p.d.f.s for large surface elevations. A semi-theoretical method is also proposed for remedying non-physical spurious oscillations that arise in the negative tail, based on the envelope of the Airy function with negative arguments. This modified negative tail is valid for irregular wave fields having skewness less than or equal to 0.2. The new p.d.f.s are compared against those based on data sets generated from second-order irregular wave theory as well as a fully nonlinear, spectrally accurate numerical wave model. Good accuracy is collectively demonstrated for directionally spread irregular seas in both finite and infinite water depths for a range of directional spreading.

Key words: coastal engineering, surface gravity waves

† Email address for correspondence: drfu@dtu.dk

1. Introduction

The statistical understanding of water waves is a topic of significant interest to oceanographers, physicists and engineers. Knowledge regarding the probability of encountering extreme surface elevations and wave heights is especially important e.g. in the design of marine structures, the analysis of wave loads on offshore wind turbines or oil platforms, as well as in ensuring safe maritime operations.

Methods for studying the statistical properties of irregular wave fields include analysis of e.g. second-order irregular waves (e.g. Forristall 2000), laboratory experiments (e.g. Onorato *et al.* 2009; Toffoli *et al.* 2010; Lawrence, Trulsen & Gramstad 2022), field measurements (e.g. Karmpadakis, Swan & Christou 2020) or numerical models (e.g. Socquet-Juglard *et al.* 2005; Toffoli *et al.* 2009; Xiao *et al.* 2013; Klahn, Madsen & Fuhrman 2021*a*,*b*; Tang & Adcock 2021; Zhang & Benoit 2021; Liu *et al.* 2022; Tang *et al.* 2022). These are, of course, in addition to theoretical means (e.g. Longuet-Higgins 1963; Song & Wu 2000), which have often been developed under simplifying narrow-band approximations and/or unidirectional assumptions (e.g. Longuet-Higgins 1952; Tayfun 1980; Tayfun & Alkhalidi 2020).

Among the most fundamentally important statistical descriptions of an irregular sea is the probability density function (p.d.f.) of the free surface elevation itself. Presently, the predominant means for theoretically computing this p.d.f. for a nonlinear, irregular gravity water wave field, free of assumptions involving narrow-bandedness and small directionality, remains the classical solution of Longuet-Higgins (1963), hereafter referred to as LH63. Utilizing the inverse Fourier transform of the cumulant generating function, LH63 derived an approximation of the resulting p.d.f. in the form of a Gram–Charlier series. To leading order his result is Gaussian, whereas his approximate distribution accounts for the leading-order effects of both skewness (beginning at second order) and kurtosis (beginning at third order).

In the present paper, we shall re-visit the classical derivation of the probability density of the surface elevation in irregular seas, to second order in the wave steepness. To the order retained, p.d.f.s will be derived from both moment and cumulant generating functions. It will be shown that, although his derivation was based on the cumulant generating function, the approximation arrived at by LH63, in fact, corresponds to that from the moment generating function. By invoking a change in variables, coupled with complex analysis, it will be newly shown that the p.d.f. stemming from the cumulant generating function can, in fact, be formulated exactly, rather than approximately, in terms of the Airy Ai function. It will be shown that this new p.d.f. exhibits a heavier positive tail than those of LH63 i.e. increased probability density of large surface elevations. A practical means for remedying spurious non-physical oscillations which arise in the probability density of negative surface elevations will likewise be devised, valid for irregular wave fields having skewness less than or equal to approximately 0.2. The resulting p.d.f.s will be compared with those based on results generated from both second-order irregular wave theory (Madsen & Fuhrman 2012) as well as from fully nonlinear, spectrally accurate numerical simulations, utilizing the model of Klahn, Madsen & Fuhrman (2021*c*).

The remainder of this paper is organized as follows: p.d.f.s to second order in the wave steepness are first derived in § 2, utilizing both moment and cumulant generating functions. The relationship to the p.d.f. of LH63 is discussed in § 3. Asymptotic limits of the p.d.f.s for large surface elevations are provided and compared in § 4. Practical considerations regarding implementation of the new p.d.f. are discussed in § 5, including a semi-theoretical means of remedying spurious oscillations in the negative tail. The accuracy of the new p.d.f.s is tested in § 6, with a practical example application based on sample data provided in § 7. Conclusions are finally drawn in § 8.

2. Probability density functions derived from moment and cumulant generating functions

Let η denote the free surface elevation and σ its standard deviation, with $\zeta \equiv \eta/\sigma$. In the form of a Stokes-type perturbation series ζ can be represented as

$$\zeta = \zeta_1 + \zeta_2 + \cdots, \tag{2.1}$$

in which the first-order wave field, ζ_1, is $O(1)$, the second-order correction, ζ_2, is $O(\varepsilon)$, and so forth, where ε is a a characteristic wave steepness. In the following sections, we derive the p.d.f. of ζ using both its moment and cumulant generating functions to second order in the wave steepness, by which we mean that we retain all terms that are $O(1)$ and $O(\varepsilon)$, but neglect all terms proportional to ε^n with $n \geqslant 2$. We assume that the coordinate system is chosen such that ζ has zero mean.

2.1. *The second-order p.d.f. of ζ derived from the moment generating function*

The moment generating function of ζ, $M_\zeta(s)$, is defined as

$$M_\zeta(s) \equiv \langle \exp(\zeta s) \rangle, \tag{2.2}$$

where s is a dimensionless (possibly complex) variable and $\langle \cdot \rangle$ denotes the expectation operator. Letting $p(\zeta)$ denote the p.d.f. of ζ and substituting is for s gives the integral equation

$$M_\zeta(\mathrm{i}s) = \int_{-\infty}^{\infty} \exp(\mathrm{i}\zeta s) p(\zeta)\, \mathrm{d}\zeta, \tag{2.3}$$

which is readily inverted for $p(\zeta)$ by means of the inverse Fourier transform

$$p(\zeta) = \frac{1}{2\pi} \int_{-\infty}^{\infty} M_\zeta(is) \exp(-\mathrm{i}\zeta s)\, \mathrm{d}s. \tag{2.4}$$

Thus, it is seen that one way to obtain the p.d.f. of a random variable is through the inverse Fourier transform of its moment generating function. Now, to compute the moment generating function of ζ, we make use of its power series form

$$M_\zeta(s) = \sum_{q=0}^{\infty} \frac{s^q}{q!} \langle \zeta^q \rangle, \tag{2.5}$$

which can be derived by Taylor expanding the exponential function in (2.2) and exploiting the linearity of the expectation operator. To compute the moments we will consider the cases where q is even and odd separately.

When q is even we may write $q = 2m$, where m is a non-negative integer, and hence

$$\langle \zeta^q \rangle = \langle \zeta^{2m} \rangle = \langle (\zeta_1 + \zeta_2)^{2m} \rangle \tag{2.6}$$

upon using (2.1). The binomial theorem then gives that

$$\langle \zeta^q \rangle = \sum_{n=0}^{2m} \binom{2m}{n} \langle \zeta_1^{2m-n} \zeta_2^n \rangle, \tag{2.7}$$

where $\binom{2m}{n}$ is the $2m$ choose n binomial coefficient. Assuming ζ_1 to be a linear combination of sine waves with random, independent phases implies that any term

containing an odd power of ζ_1 vanishes. By additionally assuming their frequencies to be densely distributed, to second order in the wave steepness, we have

$$\langle \zeta^q \rangle = \langle \zeta_1^{2m} \rangle = \frac{(2m)!}{2^m m!} \langle \zeta_1^2 \rangle^m = \frac{(2m)!}{2^m m!}, \tag{2.8}$$

where the second equality above may be shown to hold using arguments identical to those used by e.g. LH63 (see e.g. his p. 462) in addition to Song & Wu (2000) or Klahn *et al.* (2021*a*) (their § 4.1.1). The last equality follows from the fact that ζ, by definition, has unit variance i.e. to second order $\langle \zeta^2 \rangle = \langle \zeta_1^2 \rangle = 1$. We note that the even moments are $O(1)$.

When q is odd we may instead write $q = 2m + 1$, and using the same arguments as above, we find that

$$\langle \zeta^q \rangle = \langle \zeta^{2m+1} \rangle = (2m + 1) \langle \zeta_1^{2m} \zeta_2 \rangle \tag{2.9}$$

when keeping the terms consistent with the second-order approximation. Again using a calculation analogous to that of Song & Wu (2000) (see their Appendix), this result may further be shown to be

$$\langle \zeta^q \rangle = \frac{(2m + 1)!}{2^{m-1}(m - 1)!} \frac{\mathcal{S}}{6}, \tag{2.10}$$

where it has been used that, to second order, the skewness is $\mathcal{S} \equiv \langle \zeta^3 \rangle = 3 \langle \zeta_1^2 \zeta_2 \rangle$, which we note is $O(\varepsilon)$. Combining the even and odd moments with the power series form of the moment generating function (2.5), and shifting indices in the odd terms, then gives

$$M_\zeta(s) = \sum_{q=0}^{\infty} \frac{1}{q!} \left(\frac{s^2}{2} \right)^q \left(1 + \frac{1}{6} \mathcal{S} s^3 \right) = \exp\left(\frac{s^2}{2} \right) \left(1 + \frac{1}{6} \mathcal{S} s^3 \right). \tag{2.11}$$

It now follows from (2.4) that, to second order in the wave steepness, the moment generating function predicts the p.d.f. of the surface elevation to be

$$p(\zeta) = \frac{1}{2\pi} \int_{-\infty}^{\infty} \exp\left(-\frac{1}{2}(s^2 + \mathrm{i}\zeta s) \right) \left(1 + \frac{1}{6} \mathcal{S} (\mathrm{i}s)^3 \right) \mathrm{d}s. \tag{2.12}$$

Upon integrating, the result is

$$p(\zeta) = \frac{1}{\sqrt{2\pi}} \exp\left(-\frac{\zeta^2}{2} \right) \left(1 + \frac{1}{6} \mathcal{S} (\zeta^3 - 3\zeta) \right). \tag{2.13}$$

This concludes our derivation of the p.d.f. of the surface elevation based on the moment generating function.

Interestingly, the resulting expression for $p(\zeta)$ above was also found to second order by LH63, who based his derivation on the cumulant generating function, rather than the moment generating function utilized above. His derivation will be briefly reviewed and discussed further in § 3.

2.2. *The second-order p.d.f. of ζ derived from the cumulant generating function*

From the above it is seen that obtaining the p.d.f. of ζ from its moment generating function requires the calculation of an infinite number of moments. This is due to the fact that each moment, in general, consists of a first-order contribution, a second-order contribution and

so on. In that regard utilizing the cumulant generating function of ζ, $C_\zeta(s)$ is much simpler, as its terms are ordered in powers of ε. It is defined as

$$C_\zeta(s) \equiv \ln\left(M_\zeta(s)\right). \tag{2.14}$$

Moreover, the cumulants of ζ correspond directly to the coefficients C_q in the Taylor expansion

$$C_\zeta(s) = \sum_{q=1}^{\infty} \frac{C_q}{q!} s^q. \tag{2.15}$$

Upon insertion of the power series form of the moment generating function (2.5) into (2.14), and then Taylor expanding the logarithm, one finds that the first three cumulants are

$$C_1 = \langle\zeta\rangle = 0, \tag{2.16a}$$

$$C_2 = \langle\zeta^2\rangle - \langle\zeta\rangle^2 = 1, \tag{2.16b}$$

$$C_3 = \langle\zeta\rangle^3 - 3\langle\zeta^2\rangle\langle\zeta\rangle + 2\langle\zeta\rangle^3 = \mathcal{S}, \tag{2.16c}$$

and that all other cumulants are $O(\varepsilon^2)$ or smaller. To second order in the wave steepness the cumulant generating function thus reads

$$C_\zeta(s) = \tfrac{1}{2}s^2 + \tfrac{1}{6}\mathcal{S}s^3. \tag{2.17}$$

Combining this result with (2.14) and (2.4) then implies that

$$p(\zeta) = \frac{1}{2\pi}\int_{-\infty}^{\infty} \exp\left(-\frac{1}{2}s^2 + \mathrm{i}\zeta s + \frac{\mathrm{i}}{6}\mathcal{S}s^3\right)\mathrm{d}s, \tag{2.18}$$

where it has been utilized that the sign of imaginary terms within the exponential may be freely reversed without modifying the integral. To work out the integral, we start by making a change of variables. Setting

$$s = \left(\frac{2}{\mathcal{S}}\right)^{1/3}\tau - \frac{\mathrm{i}}{\mathcal{S}} \tag{2.19}$$

transforms the integral to

$$p(\zeta) = \frac{1}{2\pi}\left(\frac{2}{\mathcal{S}}\right)^{1/3}\exp\left(\frac{1}{3\mathcal{S}^2} + \frac{\zeta}{\mathcal{S}}\right)\int_{-\infty+\mathrm{i}\gamma}^{\infty+\mathrm{i}\gamma}\exp\left(\mathrm{i}\left(\frac{\tau^3}{3} + \chi\tau\right)\right)\mathrm{d}\tau, \tag{2.20}$$

in which

$$\gamma = \frac{1}{2^{1/3}\mathcal{S}^{2/3}} \tag{2.21}$$

and

$$\chi = \left(\frac{2}{\mathcal{S}}\right)^{1/3}\left(\frac{1}{2\mathcal{S}} + \zeta\right) \tag{2.22}$$

are introduced for notational convenience. Now, (2.20) is a contour integral in the complex plane with the contour being a straight line lying a distance γ above the real line.

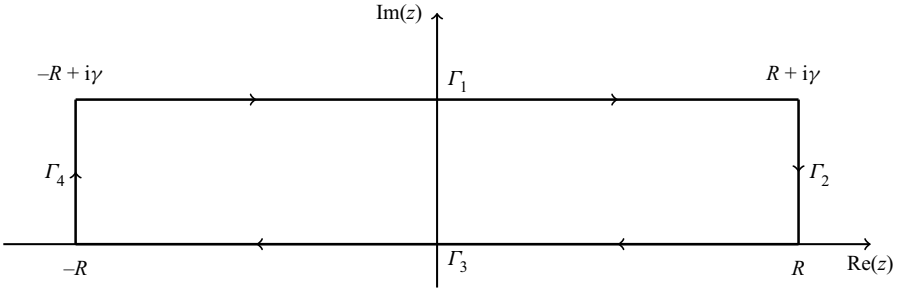

Figure 1. The contour $\Gamma = \cup_{n=1}^{4} \Gamma_n$, which should be considered in the limit where R tends to ∞. The arrows indicate the direction of integration along the segments.

However, as we will now show, the contour can be pushed down to the real line. To demonstrate this, consider the contour integral

$$\int_{\Gamma} \exp\left(\mathrm{i}\left(\frac{z^3}{3} + \chi z\right)\right) \mathrm{d}z = \sum_{n=1}^{4} \underbrace{\int_{\Gamma_n} \exp\left(\mathrm{i}\left(\frac{z^3}{3} + \chi z\right)\right) \mathrm{d}z}_{I_n} \equiv \sum_{n=1}^{4} I_n, \tag{2.23}$$

where the contour Γ, and its sub-contours, are defined in figure 1 and should be considered in the limit $R \to \infty$. Since the integrand is analytic, the residue theorem implies that the integral along Γ is exactly zero (see e.g. Berg 2013) for any value of R. Hence, if it can be proved that I_2 and I_4 vanish when R becomes large, we will have shown that (2.20) may, in fact, be evaluated by integrating along the real line. Considering I_2 first, it is clear that

$$|I_2| = \left| \int_{\Gamma_2} \exp\left(\mathrm{i}\left(\frac{z^3}{3} + \chi z\right)\right) \mathrm{d}z \right| \leqslant \int_{\Gamma_2} \left| \exp\left(\mathrm{i}\left(\frac{z^3}{3} + \chi z\right)\right) \right| \mathrm{d}z. \tag{2.24}$$

If we parameterize Γ_2 letting $z(\delta) = R + i\gamma(1-\delta)$ with $0 \leqslant \delta \leqslant 1$, and utilize the fact that γ is positive, this leads directly to

$$|I_2| \leqslant \gamma \int_0^1 \exp\left(-\gamma\left(R^2 + \chi\right)(1-\delta) + \frac{\gamma^3}{3}(1-\delta)^3\right) \mathrm{d}\delta. \tag{2.25}$$

Now, since $(1-\delta)^3 \leqslant (1-\delta)$ over the range of δ considered, we may replace the former with the latter in the final (positive) term within the exponential. This then yields that

$$|I_2| \leqslant \gamma \int_0^1 \exp\left(-\gamma\left(R^2 + \chi - \frac{\gamma^2}{3}\right)(1-\delta)\right) \mathrm{d}\delta, \tag{2.26}$$

and working out the integral then gives that

$$|I_2| \leqslant \frac{1 - \exp(-\gamma(R^2 + \chi - \gamma^2/3))}{R^2 + \chi - \gamma^2/3}, \tag{2.27}$$

and hence

$$|I_2| \leqslant \frac{1}{R^2 + \chi - \gamma^2/3}, \tag{2.28}$$

whose limit is zero as $R \to \infty$. We have thus shown that I_2 vanishes in this limit. As an identical argument can be used to show that I_4 also becomes negligible when R becomes

large, we do not present it here, but conclude that the contour in (2.23) can indeed be pushed down to the real line. Doing so yields

$$p(\zeta) = \frac{1}{2\pi}\left(\frac{2}{\mathcal{S}}\right)^{1/3} \exp\left(\frac{1}{3\mathcal{S}^2} + \frac{\zeta}{\mathcal{S}}\right) \int_{-\infty}^{\infty} \exp\left(\mathrm{i}\left(\frac{\tau^3}{3} + \chi\tau\right)\right) \mathrm{d}\tau. \tag{2.29}$$

Since the argument of the exponential function in the integrand is an odd function of τ, using the polar form of the integrand gives

$$p(\zeta) = \frac{1}{\pi}\left(\frac{2}{\mathcal{S}}\right)^{1/3} \exp\left(\frac{1}{3\mathcal{S}^2} + \frac{\zeta}{\mathcal{S}}\right) \int_{0}^{\infty} \cos\left(\frac{\tau^3}{3} + \chi\tau\right) \mathrm{d}\tau. \tag{2.30}$$

This may be equivalently written as

$$p(\zeta) = \left(\frac{2}{\mathcal{S}}\right)^{1/3} \exp\left(\frac{1}{3\mathcal{S}^2} + \frac{\zeta}{\mathcal{S}}\right) \mathrm{Ai}(\chi), \tag{2.31}$$

where

$$\mathrm{Ai}(\chi) \equiv \frac{1}{\pi}\int_{0}^{\infty} \cos\left(\frac{\tau^3}{3} + \chi\tau\right) \mathrm{d}\tau \tag{2.32}$$

defines the integral representation of the Airy function of the first kind, which is explicitly available in most any mathematical software or programming language.

The result found in (2.31) is new, and seemingly corresponds to the first time the second-order p.d.f. has been derived from the cumulant generating function, without resorting to any further approximation.

2.3. *Asymptotic equivalence of the two approaches for small steepness*

At first glance, the p.d.f.s derived from the moment (2.13) and cumulant generating functions (2.31) appear quite different. However, they are both second-order approximations of the exact p.d.f., and it is therefore natural to expect that they become equivalent in the limit of small wave steepness. In this section we demonstrate that this is indeed the case by showing that (2.31) reduces to (2.13) when ε is small.

To do so, we start by noting that, when ε is small, $\mathcal{S}$ becomes small, and hence χ becomes large. For large, positive and real arguments (see e.g. Abramowitz & Stegun 1964) the asymptotic form of the Airy function is

$$\mathrm{Ai}(\chi) \sim \frac{1}{2\pi^{1/2}\chi^{1/4}} \exp\left(-\frac{2}{3}\chi^{3/2}\right) \sum_{n=0}^{\infty} \frac{\left(-\frac{3}{4}\right)^n \Gamma\left(n+\frac{5}{6}\right)\Gamma\left(n+\frac{1}{6}\right)}{2\pi n!\chi^{3n/2}}. \tag{2.33}$$

Since $\chi \sim \varepsilon^{-4/3}$ in the limit $\varepsilon \to 0$, the nth term in the series is asymptotically of order ε^{2n}. For consistency with the assumption made in the previous section, we only retain

terms up to $O(\varepsilon)$, and by using that $\Gamma(5/6)\Gamma(1/6) = 2\pi$, we obtain

$$\mathrm{Ai}(\chi) = \frac{1}{2\pi^{1/2}\chi^{1/4}} \exp\left(-\frac{2}{3}\chi^{3/2}\right) + O(\varepsilon^2). \tag{2.34}$$

Now, a first-order Taylor series expansion in $\mathcal{S}$ of $(1 + 2\mathcal{S}\zeta)^{-1/4}$ yields

$$\frac{1}{2\pi^{1/2}\chi^{1/4}} = \frac{1}{\sqrt{2\pi}}\left(\frac{2}{\mathcal{S}}\right)^{-1/3}\left(1 - \frac{1}{2}\mathcal{S}\zeta + O(\varepsilon^2)\right). \tag{2.35}$$

Moreover, from a third-order Taylor series expansion of $(1 + 2\mathcal{S}\zeta)^{3/2}$ it follows that

$$\begin{aligned}\exp\left(-\frac{2}{3}\chi^{3/2}\right) &= \exp\left(-\frac{1}{3\mathcal{S}^2}\left(1 + 3\mathcal{S}\zeta + \frac{3}{2}\mathcal{S}^2\zeta^2 - \frac{1}{2}\mathcal{S}^3\zeta^3 + O(\varepsilon^4)\right)\right) \\ &= \exp\left(-\frac{1}{3\mathcal{S}^2} - \frac{\zeta}{\mathcal{S}} - \frac{\zeta^2}{2}\right)\left(1 + \frac{\mathcal{S}}{6}\zeta^3 + O(\varepsilon^2)\right).\end{aligned} \tag{2.36}$$

Hence, we may rewrite the asymptotic approximation of the Airy function as

$$\mathrm{Ai}(\chi) = \frac{1}{\sqrt{2\pi}}\left(\frac{2}{\mathcal{S}}\right)^{-1/3}\exp\left(-\frac{1}{3\mathcal{S}^2} - \frac{\zeta}{\mathcal{S}} - \frac{\zeta^2}{2}\right)\left(1 + \frac{\mathcal{S}}{6}(\zeta^3 - 3\zeta) + O(\varepsilon^2)\right). \tag{2.37}$$

Inserting this into (2.31), we then find that

$$p(\zeta) = \frac{1}{\sqrt{2\pi}}\exp\left(-\frac{\zeta^2}{2}\right)\left(1 + \frac{\mathcal{S}}{6}(\zeta^3 - 3\zeta) + O(\varepsilon^2)\right), \tag{2.38}$$

which matches the result seen in (2.13). Thus, we have shown that the second-order results implied by the moment and cumulant generating functions are asymptotically equivalent in the limit of small wave steepness. Obviously, both reduce to the Gaussian (normal) distribution

$$p(\zeta) = \frac{1}{\sqrt{2\pi}}\exp\left(-\frac{\zeta^2}{2}\right) \tag{2.39}$$

in the linear limit.

3. Discussion of Longuet-Higgins (1963)

LH63 based the derivation of his p.d.f. on the cumulant generating function, carried out to one order higher than in § 2.2. We will here briefly review the derivation of his result, with the aim of establishing the relationship to those derived above. Following the procedure outlined in § 2.2, but carried out to third order (see LH63 for details), (2.18) becomes

$$p(\zeta) = \frac{1}{2\pi}\int_{-\infty}^{\infty}\exp\left(-\frac{1}{2}s^2 + \mathrm{i}\zeta s + \frac{\mathrm{i}}{6}\mathcal{S}s^3 + \frac{\mathcal{K}-3}{24}s^4\right)\mathrm{d}s, \tag{3.1}$$

where $\mathcal{K} \equiv \langle\zeta^4\rangle$ is the kurtosis. LH63 conceptually divided the integrand as

$$p(\zeta) = \frac{1}{2\pi}\int_{-\infty}^{\infty}\exp\left[-\frac{1}{2}s^2 + \mathrm{i}\zeta s\right]\exp\left[\frac{\mathrm{i}\mathcal{S}}{6}s^3 + \frac{\mathcal{K}-3}{24}s^4\right]\mathrm{d}s, \tag{3.2}$$

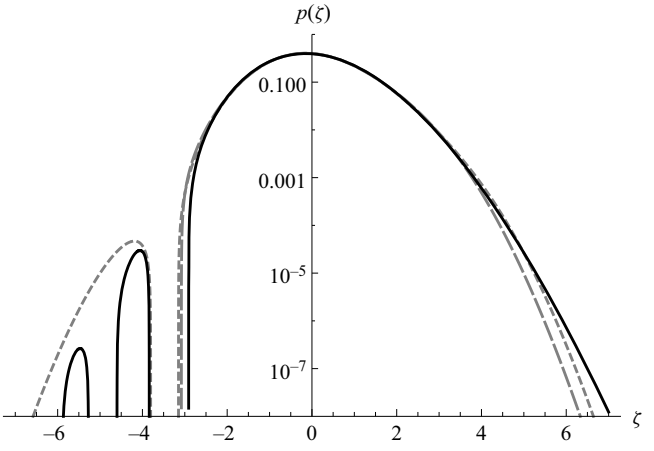

Figure 2. Comparison of the p.d.f. from (2.31) (full line) with the second- (dashed line) and third-order (dotted line) approximations of LH63, from (3.4). All cases use $\mathcal{S} = 0.30$, with the LH63 third-order result additionally using $\mathcal{K} = 3.1$. Note the non-physical oscillations for $\zeta \lesssim -2.8$ exhibited by all three distributions.

and subsequently replaced the second exponential with its Taylor series. This leads to the approximation

$$p(\zeta) = \frac{1}{2\pi}\int_{-\infty}^{\infty} \exp\left[-\frac{1}{2}s^2 + \mathrm{i}\zeta s\right]\left[1 + \frac{\mathrm{i}\mathcal{S}}{6}s^3 + \left\{\frac{\mathcal{K}-3}{24}s^4 - \frac{\mathcal{S}^2}{72}s^6\right\}\right]\mathrm{d}s. \tag{3.3}$$

After integrating, his final result takes the form of a Gram–Charlier series

$$p(\zeta) = \frac{1}{\sqrt{2\pi}}\exp\left(-\frac{\zeta^2}{2}\right)\left[1 + \frac{\mathcal{S}}{6}H_3 + \left\{\frac{\mathcal{K}-3}{24}H_4 + \frac{\mathcal{S}^2}{72}H_6\right\}\right], \tag{3.4}$$

where

$$H_3 = \zeta^3 - 3\zeta, \tag{3.5a}$$

$$H_4 = \zeta^4 - 6\zeta^2 + 3, \tag{3.5b}$$

$$H_6 = \zeta^6 - 15\zeta^4 + 45\zeta^2 - 15, \tag{3.5c}$$

are Hermite polynomials. Note that the term proportional to $\mathcal{S}$ is $O(\varepsilon)$, whereas the terms within the curly braces are $O(\varepsilon^2)$.

It is important to emphasize that (3.4) is only an approximation of (3.1), even to second order. The reason is that the Taylor series expansion introduced within the integrand of (3.3) will only be accurate for small $|s|$, and not over the entire interval $-\infty \leqslant s \leqslant \infty$. As was mentioned in § 2.2, to second order the result of LH63 above, in fact, matches the p.d.f. derived from the moment generating function, rather than from the cumulant generating function on which it is based. It turns out that his final result is only asymptotic to our result given in (2.31).

Comparison of the p.d.f.s given by (3.4) and the newly derived (2.31) are presented in figure 2, utilizing $\mathcal{S} = 0.3$ and (for the third-order result of LH63) $\mathcal{K} = 3.1$. These values have been chosen to be reasonably representative of a typical nonlinear, irregular sea in intermediate depth to deep water, see e.g. figure 2 of Klahn *et al.* (2021*b*), as well as in tables 1 and 2 (see § 6). It is seen that the present (second-order) method predicts increased

probability density of extreme positive ζ relative to both the second- and third-order approaches of LH63. This heavy tail will be investigated and explained in the next section. It is likewise seen that all of the distributions shown suffer from non-physical oscillations for moderate to large, negative ζ. The failure in this region implies that these p.d.f.s cannot be utilized to reliably predict the probability density of the surface elevation in moderate to extreme wave trough regions. A semi-theoretical means of remedying this deficiency in (2.31) is developed in § 5.1, valid for weakly nonlinear situations having sufficiently small skewness.

4. Asymptotic limits of the p.d.f.s for large surface elevations

The example depicted in figure 2 demonstrates that the new second-order p.d.f. (2.31) has a heavier tail than both the second- and third-order results of LH63. This can be explained by inspection of their asymptotic forms for large surface elevations. As $\zeta \to \infty$, our new p.d.f. (2.31) tends asymptotically to

$$p(\zeta) \sim \frac{1}{2^{3/4}\sqrt{\pi}(\mathcal{S}\zeta)^{1/4}} \exp\left(\frac{1}{3\mathcal{S}^2} - \frac{1}{8\sqrt{2\zeta}\mathcal{S}^{5/2}} - \frac{\sqrt{\zeta}}{\sqrt{2}\mathcal{S}^{3/2}} + \frac{\zeta}{\mathcal{S}} - \frac{2\sqrt{2}\zeta^{3/2}}{3\sqrt{\mathcal{S}}}\right). \quad (4.1)$$

Conversely, the second- and third-order p.d.f.s of LH63 (see present (3.4)), respectively, tend asymptotically to

$$p(\zeta) \sim \frac{\mathcal{S}\zeta^3}{6} \frac{1}{\sqrt{2\pi}} \exp\left(-\frac{\zeta^2}{2}\right) \quad (4.2)$$

and

$$p(\zeta) \sim \frac{\mathcal{S}^2\zeta^6}{72} \frac{1}{\sqrt{2\pi}} \exp\left(-\frac{\zeta^2}{2}\right). \quad (4.3)$$

These asymptotic forms are plotted in figure 3, along with the Gaussian distribution (2.39). For consistency with figure 2, with the exception of the Gaussian distribution, all cases use $\mathcal{S} = 0.3$. Note that the asymptotic form of the third-order LH63 result (4.3) involves $\mathcal{S}^2$, and not $\mathcal{K}$. Notice that the asymptotic forms stemming from LH63's result, (4.2) and (4.3), are merely factors of $\mathcal{S}\zeta^3/6$ and $\mathcal{S}^2\zeta^6/72$ times the Gaussian distribution (2.39), both having argument $-\zeta^2/2$ in the exponential function. As these match that of the Gaussian distribution, their positive tails are likewise similar, essentially being just vertically shifted when plotted on semi-logarithmic axes. Conversely, the asymptotic limit of the present new p.d.f. is fundamentally different. In particular, it is noted that all powers of ζ within the argument of the exponential function in (4.1) are less than the power 2 of the Gaussian distribution, the largest power being 3/2. This explains the heavier positive tail exhibited by the present new p.d.f. (2.31), relative to those of LH63 from (3.4).

It is emphasized that the heavy tail, and any associated increased accuracy (see forthcoming § 6), exhibited by the present second-order p.d.f., relative e.g. even to the third-order result of LH63, would not be in violation of any theory. The formal order of a given method only governs its asymptotic rate of convergence in the limit of small steepness; higher formal order does not necessarily imply greater accuracy. Indeed, as shown in § 2.3, the differences between the new second-order p.d.f. (2.31) and the second-order result of LH63, which again matches (2.13), are themselves of third order. This section establishes that a heavy tail is inherent within the new second-order p.d.f. (2.31) and is among these differences.

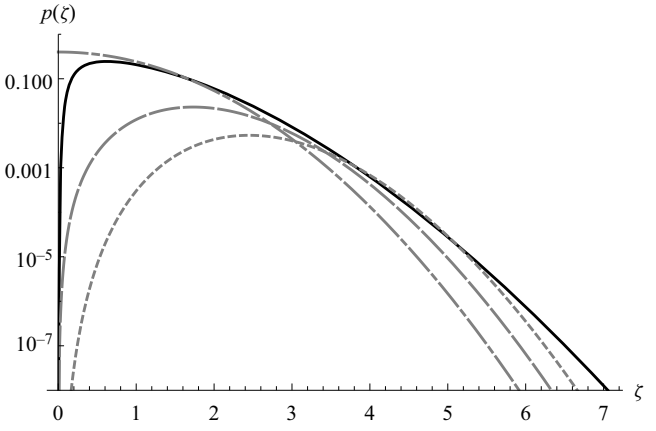

Figure 3. Comparison of the asymptotic forms (as $\zeta \to \infty$) of the p.d.f.s. Lines correspond to the present second-order theory (4.1) (full line), the second- (4.2) (dashed line) and third-order (4.3) (dotted line) approximations of LH63, as well as the Gaussian distribution (2.39) (dashed-dotted line). With the exception of the Gaussian distribution, all cases use $\mathcal{S} = 0.30$. Note the heavy tail exhibited by the present distribution (full line).

5. Practical considerations

5.1. *Removal of spurious oscillations in the negative tail*

As shown in figure 2 (full line), for finite $\mathcal{S}$ and moderate to large, negative ζ, the p.d.f. given in (2.31) results in spurious oscillations, and even negative probability densities. Such features can obviously be dismissed as non-physical. A semi-theoretical method for addressing the oscillations inherent in (2.31), valid for small but finite $\mathcal{S}$, will be developed in the present section, inspired by inspection of the Airy functions with negative arguments. For later use within this section, note that the Airy function of the second kind is defined by

$$\mathrm{Bi}(\chi) \equiv \frac{1}{\pi}\int_0^\infty \left[\exp\left(-\frac{\tau^3}{3} + \chi\tau\right) + \sin\left(\frac{\tau^3}{3} + \chi\tau\right)\right] \mathrm{d}\tau. \tag{5.1}$$

To begin, both $\mathrm{Ai}(\chi)$ (grey dashed line) and $\mathrm{Bi}(\chi)$ (grey dotted line) are plotted in figure 4. It is additionally noted that the envelope of both Airy functions (with negative arguments) follows

$$\mathrm{Ci}(\chi) \equiv [\mathrm{Ai}(\chi)^2 + \mathrm{Bi}(\chi)^2]^{1/2}, \tag{5.2}$$

which is depicted as the full line in figure 4. The asymptotic limit as $\chi \to -\infty$, $\mathrm{Ci}(\chi) \sim \pi^{-1/2}(-\chi)^{-1/4}$, is also shown for completeness.

Inspired by the observations above, we propose the following as a suitable generalization of (2.31) for some practical purposes:

$$p(\zeta) = \left(\frac{2}{\mathcal{S}}\right)^{1/3} \exp\left[\frac{1}{3\mathcal{S}^2} + \frac{\zeta}{\mathcal{S}}\right] \mathrm{Zi}\,(\chi)\,, \tag{5.3}$$

wherein $\mathrm{Ai}(\chi)$ has been replaced with

$$\mathrm{Zi}(\chi) \equiv \begin{cases} \mathrm{Ai}(\chi) & \text{for } \chi \geqslant \chi_0 \\ \mathrm{Ci}(\chi) & \text{for } \chi < \chi_0. \end{cases} \tag{5.4}$$

To ensure smoothness of the modified p.d.f., we require that $\mathrm{Ai}(\chi_0) = \mathrm{Ci}(\chi_0)$ and $\mathrm{Ai}'(\chi_0) = \mathrm{Ci}'(\chi_0)$, both of which are satisfied at $\chi_0 \approx -1.17371$, see figure 4.

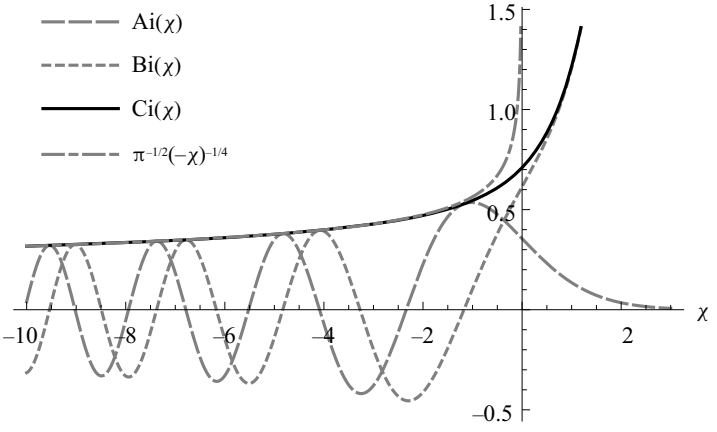

Figure 4. Plot demonstrating the behaviour of the Airy functions $\mathrm{Ai}(\chi)$ and $\mathrm{Bi}(\chi)$, their envelope $\mathrm{Ci}(\chi)$ as well as its asymptotic form $\mathrm{Ci}(\chi) \sim \pi^{-1/2}(-\chi)^{-1/4}$.

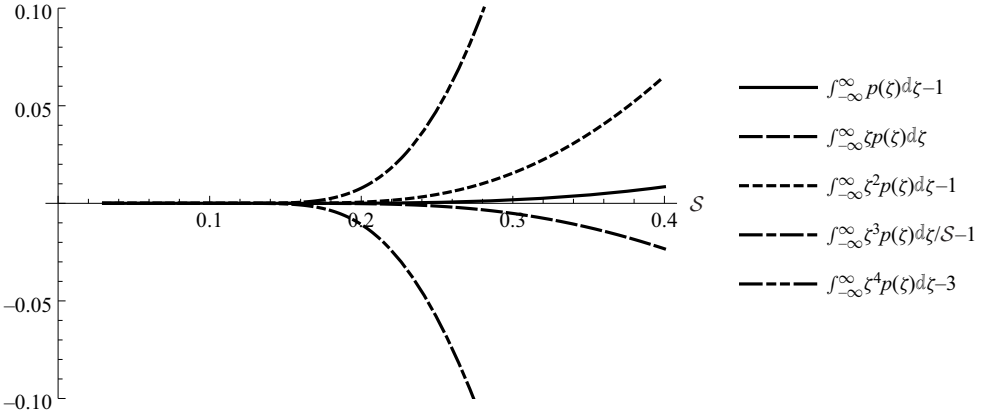

Figure 5. Integral and statistical moments computed from the modified p.d.f. (5.3). All integrals have been shifted and/or normalized as indicated in the legend, such that plotted quantities should theoretically be zero.

The modification above enables direct use of the $\mathrm{Ai}(\chi)$ function for $\chi \geqslant \chi_0$, fully consistent with the theory from (2.31). Conversely, it switches to the envelope $\mathrm{Ci}(\chi)$ for $\chi < \chi_0$, where the theoretical solution clearly breaks down.

To check the practical validity of (5.3), we plot the integral of the resulting p.d.f., as well as its first four statistical moments, vs the input skewness $\mathcal{S}$ in figure 5. All plotted quantities are thus of the general form

$$\int_{-\infty}^{\infty} \zeta^m p(\zeta)\,\mathrm{d}\zeta, \tag{5.5}$$

where $m = 0, 1, \ldots, 4$, where each is normalized and/or vertically shifted as indicated in the figure legend, such that they should theoretically be equal to zero. It is seen that for all quantities plotted reasonable accuracy is maintained for say $\mathcal{S} \lesssim 0.2$. At the upper limit $\mathcal{S} = 0.2$ the modified p.d.f. from (5.3) yields a mean of -0.00015, a variance of 1.0005, a skewness of 0.199 and a kurtosis of 3.007. These may be compared with their respective theoretical values of zero, unity, 0.2 (as input) and 3. It is emphasized that if the theoretical

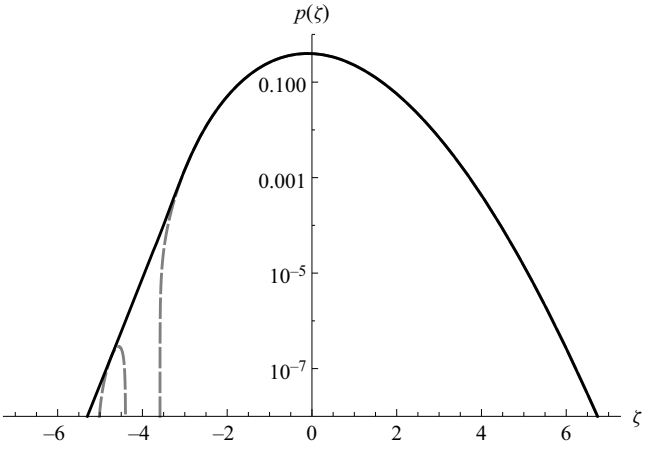

Figure 6. Comparison of p.d.f.s from (5.3) (full line) and (2.31) (dashed line), with $\mathcal{S} = 0.2$. Note the removal of spurious oscillations in the negative tail using (5.3).

p.d.f. from (2.31) is maintained then the theoretical values are matched exactly, regardless of $\mathcal{S}$.

An example using the modified p.d.f. defined in (5.3), now with $\mathcal{S} = 0.2$ (again, the upper recommended limit), can be seen as the full black line in figure 6. This result can be compared with the previously discussed result based on (2.31), which is similarly plotted as the grey dashed line in figure 6. It is seen that the two are, by design, identical for positive and moderately negative ζ. Importantly, (5.3) avoids any spurious non-physical oscillations for negative ζ, which are erroneously exhibited by (2.31).

To conclude: the theoretically derived new second-order p.d.f. corresponds to (2.31). Should it be desired, for weakly nonlinear cases having $\mathcal{S} \leqslant 0.2$, this may be replaced in practice with (5.3), which will remove spurious oscillations of the negative tail, while maintaining reasonably accurate statistical moments. The accuracy of the resulting p.d.f.s will be directly tested in § 6, where the limits in $\mathcal{S}$ suggested above will be strictly followed.

5.2. *Numerical precision*

Regarding practical issues, it should be finally mentioned that the evaluation of $\mathrm{Ai}(\chi)$ can face problems associated with loss of numerical precision, particularly when considering cases having small $\mathcal{S}$. When making calculations in double precision we find that such issues can arise whenever this argument becomes $\chi > \chi_{thresh} \approx 108$, which will return zero, rather than an extremely small number (which in turn must be multiplied by an extremely large number stemming from the exponential function, see (2.31) or (5.3)). From the definition in (2.22), this issue will manifest in $p(\zeta)$ whenever

$$\zeta \gtrsim \frac{2^{2/3}\mathcal{S}^{4/3}\chi_{thresh} - 1}{2\mathcal{S}}. \tag{5.6}$$

Fortunately, this issue is easily overcome in practice simply by ensuring that the argument χ is evaluated to high precision e.g. using vpi in Matlab or SetPrecision in Mathematica, and we recommend doing similarly for the argument of the exponential function for the sake of consistency. Such high-precision calculations have been utilized in all relevant plots presented throughout the present work. As an example implementation, a Matlab function pdfAiry.m evaluating the p.d.f. defined in (5.3) if $\mathcal{S} \leqslant 0.2$ and (2.31) otherwise

is provided at the link indicated in the Data Availability section towards the end of the present paper.

6. Comparisons

6.1. *Comparison with results from second-order irregular wave theory*

As a first means of validation we will compare the new p.d.f.s against those generated from time series utilizing the directionally spread (third-order) irregular wave theory of Madsen & Fuhrman (2012), carried out to second order. (Note that some errors unfortunately appeared in their original publication, which are pointed out for clarity in Appendix A.) For validation purposes we will consider three cases, each based on a Joint North Sea Wave Project (JONSWAP) spectrum (Hasselmann *et al.* 1973)

$$S(\omega) = S_0 \left(\frac{\omega}{\omega_p}\right)^{-5} \exp\left(-\frac{5}{4}\left(\frac{\omega}{\omega_p}\right)^{-4}\right) \gamma_s^{\exp\left(-(\omega/\omega_p-1)^2/(2\sigma_s^2)\right)}, \tag{6.1}$$

where ω is the angular frequency, ω_p is the peak angular frequency, $\gamma_s = 3.3$ and $\sigma_s = 0.07$ if $\omega < \omega_p$ and 0.09 otherwise. A cutoff frequency of $\omega_c = 3\omega_p$ is utilized, such that $S(\omega > \omega_c) = 0$. The constant S_0 is defined such that the linearized spectrum satisfies

$$\int_0^\infty S(\omega)\,\mathrm{d}\omega = \sigma^2, \tag{6.2}$$

with second-order components added afterwards. The waves are directionally spread (utilizing single summation) based on

$$D(\theta) = \begin{cases} \dfrac{\Gamma(N_D/2+1)}{\sqrt{\pi}(\Gamma(N_D+1)/2)} \cos^{N_D}(\theta) & \text{if } |\theta| \leqslant \dfrac{\pi}{2} \\ 0 & \text{otherwise,} \end{cases} \tag{6.3}$$

where $\Gamma(\cdot)$ denotes the gamma function and N_D is the directional-spreading parameter, which governs the width of the directional spectrum.

All cases utilize a finite depth such that $k_p h = 1.2$, where k_p is the peak wavenumber, determined from the dispersion relation

$$\omega_p^2 = g k_p \tanh k_p h, \tag{6.4}$$

and $h = 70$ m is the water depth, with gravitational acceleration $g = 9.81$ m s^{-2} such that the peak period is $T_p = 16.8$ s. All cases utilize the directional-spreading parameter $N_D = 50$. We will consider three cases representing storm conditions with linear steepness $\varepsilon = k_p H_{m0}/2 = 2k_p\sigma = 0.10$, 0.15 and 0.20, where H_{m0} is the spectral significant wave height. The primary purpose of the present comparisons is thus to test the performance of the new p.d.f.s for irregular wave fields having variable nonlinearity in finite depth. For each case numerous ($\approx$120 000) discrete time series segments have been independently generated, each spanning a duration $100T_p$, resolved with time step $\Delta t = T_p/20$. This means that, for each condition considered, approximately 6.4 years of storm data are collectively generated and analysed. The resulting statistics (steepness ε, variance σ^2, skewness $\mathcal{S}$ and kurtosis $\mathcal{K}$) are summarized in table 1.

ε	σ^2 (m^2)	$\mathcal{S}$	$\mathcal{K}$
0.1007	8.630	0.1879	3.038
0.1524	19.76	0.2688	3.101
0.2057	35.99	0.3355	3.190

Table 1. Summary statistics from the data generated using the second-order irregular wave theory of Madsen & Fuhrman (2012). All cases utilize finite depth $k_p h = 1.2$ and directional spreading parameter $N_D = 50$.

Selected time series segments are exemplified in figure 7, corresponding to those containing the largest crest elevation generated for each case. Insets are provided on each panel, depicting a zoomed-in region surrounding the large crests. It is seen that these selected events contain isolated rogue waves, with crest elevations in the most extreme case generated reaching nearly $\zeta = 8$. Interestingly, these extreme events are typically surrounded by otherwise rather ordinary conditions for the sea states considered, typically with $-3 \leqslant \zeta \leqslant 3$. That the extreme waves would appear to have 'come from nowhere' seems consistent with anecdotal accounts often reported by mariners and as occasionally even measured. Note e.g. the qualitative similarity with the famous 'New Year' rogue wave, measured in the North Sea on 1 January 1995 from the Draupner oil platform (water depth $h = 70$ m), similarly presented in figure 8. Based on analysis of this measured time series segment alone, the storm conditions there would correspond to $\sigma^2 \approx 8.9$ m^2, $k_p h \approx 1.2$ and $\varepsilon \approx 0.10$, similar to the input conditions leading to the event depicted in figure 7(*a*). (The close similarity in input for this case is intentional, as we were curious to see if similar peak events might indeed be generated stochastically using a second-order theory.)

For each case the numerous time series segments have been collectively analysed, with a ζ bin size corresponding to 0.2, resulting in the three p.d.f.s (circles) shown in figure 9. Error bars are also included, estimated as $\pm p(\zeta)/\sqrt{N_b}$, where N_b is the number of samples in each bin, following Onorato *et al.* (2009). Also shown for comparison are the p.d.f.s from (i) the Gaussian distribution (dotted lines), (ii) LH63 (second order: dashed lines, third order: dashed-dotted lines) and (iii) the presently proposed p.d.f.s (full lines). In line with the recommendation made in § 5.1, the modified variant (5.3) is only utilized in the case where $\mathcal{S} \leqslant 0.2$ (figure 9*a*), whereas the theoretical p.d.f. (2.31) is utilized in figure 9(*b*,*c*). It is seen that the proposed new p.d.f. provides superior accuracy to both the Gaussian distributions (expected from linear theory), as well as those of LH63, especially in the positive tail. Somewhat remarkably, and as mentioned previously, even though effects of kurtosis are not at all accounted for, the present distribution even outperforms the third-order distribution of LH63. As should be expected from § 5.1, the distribution from (5.3) (figure 9*a*) is free of spurious oscillations in the negative tail, in contrast to those of LH63 or (2.31) which fail for roughly $\zeta < -3$. The comparison in figure 9(*a*) suggests that this modification provides similar accuracy for predicting the probability density of negative surface elevations as for positive ones, at least for cases having $\mathcal{S} \leqslant 0.2$ where it can be reasonably applied. Remaining differences between the generated data and the new p.d.f.s seem likely due to neglected third-order effects in the distribution (e.g. kurtosis). Obviously, none of the methods employed account for any effects of wave breaking on the p.d.f., although there is considerable evidence that these do not necessarily have a significant impact in the probability domain, see e.g. the discussion in Tayfun & Alkhalidi (2020).

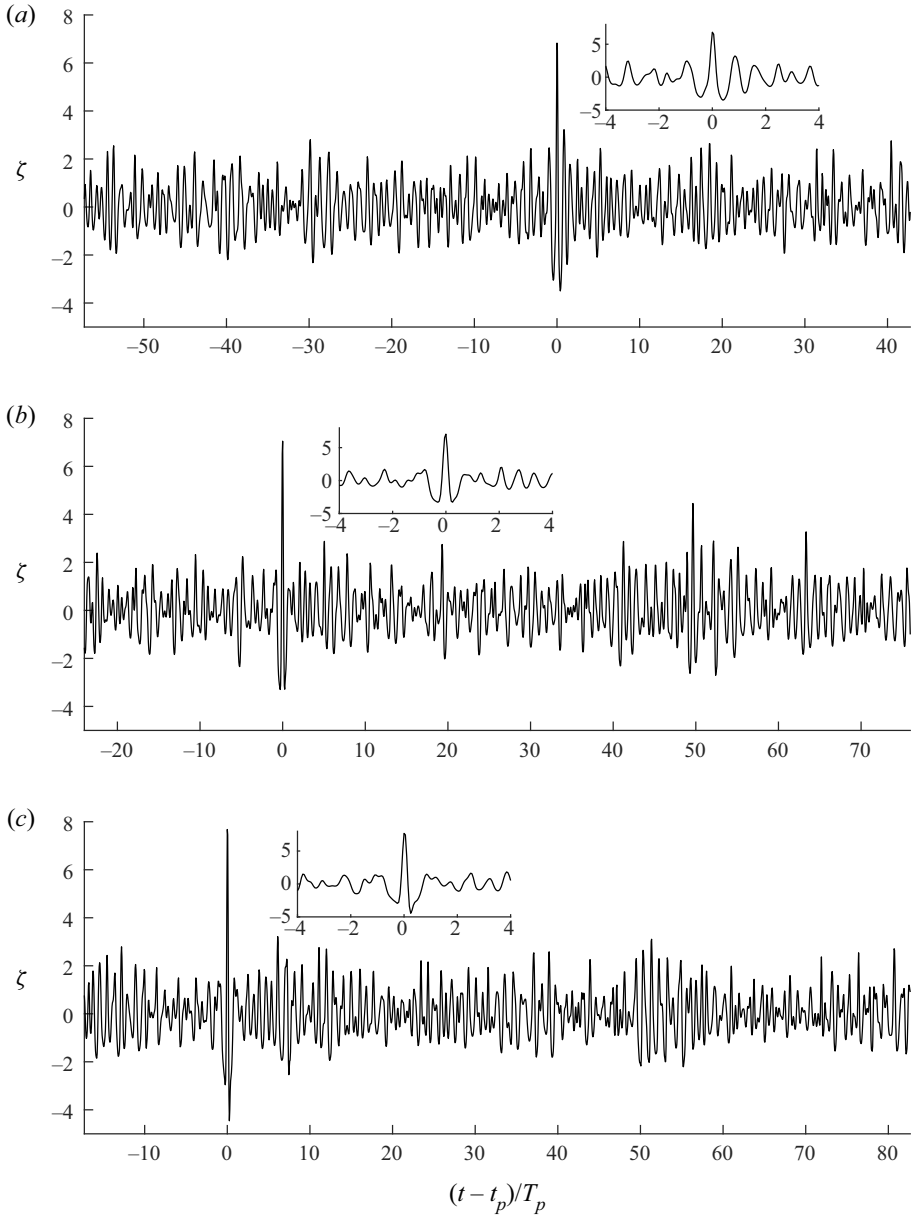

Figure 7. Example time series involving the largest crests (occurring at time $t = t_p$) generated by the irregular, directionally spread wave theory of Madsen & Fuhrman (2012) to second order. Insets depicting the region immediately surrounding the largest crest are added on each panel. Cases utilize $k_p h = 1.2$ and $N_D = 50$ coupled with linear steepness (*a*) $\varepsilon = 0.10$, (*b*) 0.15 and (*c*) 0.20.

6.2. *Comparison with results from fully nonlinear numerical simulations*

As an additional means of validation, we will consider data generated utilizing the fully nonlinear pseudospectral Fourier–Legendre (PFL) potential flow simulation model of Klahn *et al.* (2021*c*), as used previously by Klahn *et al.* (2021*a*,*b*). This model is spectrally accurate in all three spatial directions and maintains good computational efficiency.

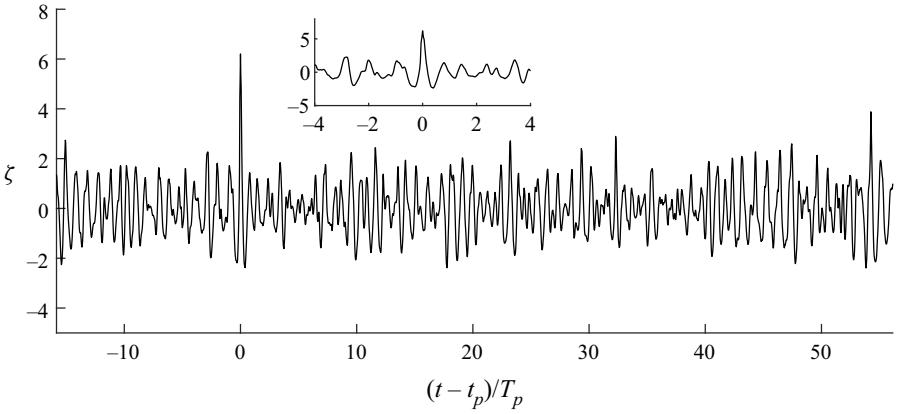

Figure 8. Time series segment containing the famous 'New Year' rogue wave measured from the Draupner oil platform in the North Sea on 1 January 1995.

This method makes use of an artificial lower boundary condition based on Nicholls (2011), with iterative solutions to the resulting Laplace equation utilizing a linearized preconditioner, following the strategy of Fuhrman & Bingham (2004). For full details on this model and features, see Klahn *et al.* (2021*a*,*b*,*c*).

We simulate irregular, directionally spread wave fields, again based on JONSWAP spectra, with $k_ph = 1.0$, 1.5 and ∞ (deep water), now utilizing the directional-spreading parameter $N_D = 2$. For all cases simulations utilize a large 2048 × 2048 (horizontal) grid, coupled with 11 points distributed in the vertical direction. The computational domain has lengths $L_x = 100\lambda_p$ and $L_y = 100(1 + N_D)^{1/2}\lambda_p$, where $\lambda_p = 2\pi/k_p = 275$ m, which provides similar resolution of wavelengths in both horizontal directions, following Klahn *et al.* (2021*a*). Note that the resolution utilized implies that the spectrum is effectively cut off at $\omega_c \approx 4.86\omega_p$, see (3.24) of Klahn *et al.* (2021*a*). The computational domains can be considered extremely large for such fully nonlinear simulations, covering a physical area corresponding to 28.2 km × 48.8 km. Starting with linearized initial conditions, the nonlinear terms are ramped to fully on over a duration of $10T_p$, following the same procedure described in Klahn *et al.* (2021*a*,*b*), and then continued for a total duration of $100T_p$. The characteristic wave steepness for the linearized initial conditions are set according to $\varepsilon = \varepsilon_0 \tanh(0.8863k_ph)$, where $\varepsilon_0 = 0.15$ is a deep water 'equivalent steepness'. This ensures that, for a given ε_0, cases in any k_ph will have roughly the same degree of nonlinearity, relative to the maximum steepness criterion of Battjes (1974). The primary purpose of the present tests is thus to compare the performance of the new p.d.f.s in irregular wave fields having similar nonlinearity, but with variable dimensionless water depth. Note that above the steepness $\varepsilon_0 = 0.15$ it becomes difficult to maintain stable nonlinear statistics, as shown e.g. in figure 2(*a*) of Klahn *et al.* (2021*b*). This is due to dissipative effects introduced through filtering, which is necessary for stability purposes when extremely steep (potentially breaking) waves are encountered. The time step is set such that $\Delta t = T_p/50$. For each case, we have carried out the time integration with five different initial conditions, with the phase of each wave component determined randomly. Each simulation considered requires several months of simulation time on a single processor. The resulting statistics (steepness ε, variance σ^2, skewness $\mathcal{S}$ and kurtosis $\mathcal{K}$), based on data accumulated from all five simulations of each case at time $t = 50T_p$, are summarized in table 2. Note that at this time the nonlinear wave fields can

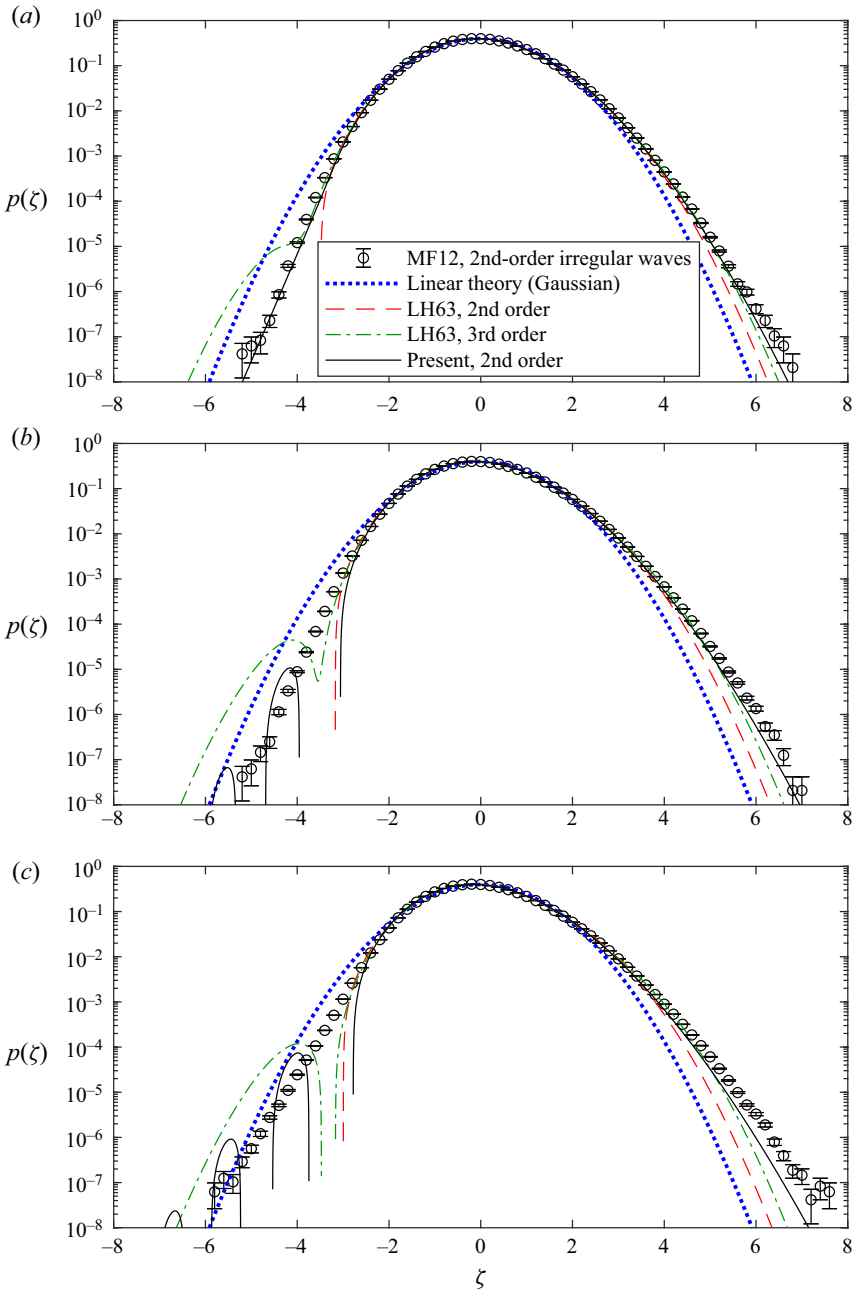

Figure 9. Comparison of p.d.f.s computed from the second-order directionally spread irregular wave theory of Madsen & Fuhrman (2012, referred to as MF12) (circles, with error bars) with (3.4) from LH63 (second order, dashed lines; third order, dashed-dotted lines) and the present work using (*a*) (5.3) and (*b*,*c*) (2.31) (full lines). Cases utilize $k_p h = 1.2$ and $N_D = 50$ coupled with (*a*) $\varepsilon = 0.1007$, (*b*) 0.1524 and (*c*) 0.2057, with other statistical quantities given in table 1.

k_ph	ε	σ^2 (m^2)	$\mathcal{S}$	$\mathcal{K}$
1.0	0.1048	5.263	0.2306	3.060
1.5	0.1270	7.726	0.1967	3.051
∞	0.1443	9.964	0.1854	3.050

Table 2. Summary statistics for the data generated from fully nonlinear numerical simulations. All cases utilize directional-spreading parameter $N_D = 2$.

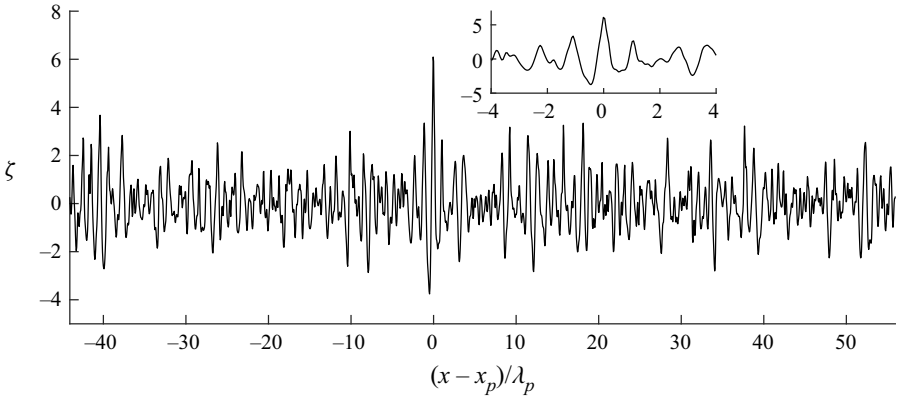

Figure 10. Example free surface elevation along the line containing the largest crest generated by the fully nonlinear wave model of Klahn *et al.* (2021*c*) for the case with $k_ph = 1.5$, $N_D = 2$ and $\varepsilon = 0.1270$. The inset depicts a zoomed-in region immediately surrounding the largest crest. Variable x_p denotes the x position of the highest crest peak.

be considered well developed, with reasonably stable statistics, as established in previous simulations performed by Klahn *et al.* (2021*a*,*b*).

An example snapshot of the computational line in x containing the largest rogue wave peak elevation generated at time $t = 50T_p$ from the simulated case with $k_ph = 1.5$ is depicted in figure 10. Reasonable similarity with the time series from figures 7(*a*) and 8 can be there observed, with the free surface again reaching $\zeta \approx 6$. A small three-dimensional segment of the simulated large domain containing this rogue wave is likewise provided in figure 11, as an example.

The resulting p.d.f.s for the surface elevations accumulated from the fully nonlinear simulations for all three cases are presented as circles (with error bars, computed as previously described) in figure 12. For each case considered it is seen that isolated rogue waves having surface elevations reaching up to the previously mentioned $\zeta \approx 6$ have been generated in each case. As references the Gaussian distribution, as well as those from LH63 (both second and third order) are additionally shown in this figure. Good accuracy is confirmed with the present method utilizing (2.31) (figure 12*a*) and (5.3) (figure 12*b*,*c* as $\mathcal{S} \leqslant 0.2$) (full lines). The heavy positive tail associated with the present method is again evident, and is closer to the data than even the third-order distribution of LH63. In cases where the modified variant (5.3) has been utilized (again, figure 12*b*,*c*) oscillations in the negative tails are removed and the result matches the data reasonably. Based on these comparisons, it seems that the new p.d.f.s given in (2.31) or (5.3) (provided that $\mathcal{S} \leqslant 0.2$) are appropriate for practical use.

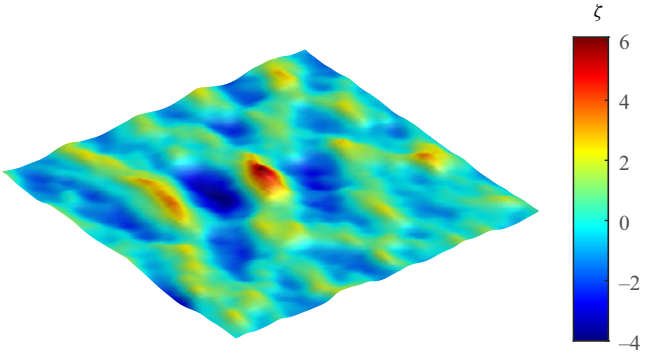

Figure 11. Snapshot of the surface elevation in the vicinity of the largest rogue wave crest generated by the fully nonlinear model of Klahn *et al.* (2021*c*) for the case with $k_ph = 1.5$, $N_D = 2$ and $\varepsilon = 0.1270$. The horizontal axes are to scale, whereas the vertical axis is exaggerated by a factor of two. The horizontal area shown is $4\lambda_p \times 4\lambda_p$.

7. Example application of the new p.d.f. using sample data

It is clear that application of the new theoretical p.d.f. (2.31), or (if applicable) the variant with modified negative tail (5.3), requires that the skewness of the wave field be known. Likewise, knowing the skewness and kurtosis is a prerequisite for respectively applying the second- and third-order result of LH63 from (3.4). As these quantities must often be estimated from sample data (from e.g. numerical simulations or experimental or field measurements) in practice, an obvious question is: Does it actually make sense to estimate the required statistics from sample data and use them in combination with the desired p.d.f.? After all, it may be argued that one could simply estimate the p.d.f. directly from the sampled data.

To answer this question, suppose we have a record consisting of n uncorrelated samples of the surface elevation. It is well known that the standard deviation of the skewness and the kurtosis (assuming Gaussian data and large sample size) are approximately $\sigma_{\mathcal{S}} = \sqrt{6/n}$ and $\sigma_{\mathcal{K}} = \sqrt{24/n}$, respectively, dating back to Fisher (1930). Due to their $n^{-1/2}$ dependence, it appears that the uncertainties of the skewness and kurtosis decrease quite slowly, and that this might carry over to the distribution when used e.g. with the sample estimate of the skewness. However, the value of n needed to bring $\sigma_{\mathcal{S}}$ and $\sigma_{\mathcal{K}}$ down to, say, a few per cent of $\mathcal{S}$ and $\mathcal{K}$, respectively, is in fact not excessively large, and at this level of uncertainty the p.d.f.s are rather insensitive to associated uncertainties. Moreover, the uncertainty of the sampled distribution would typically be much larger, especially in the tails which will inevitably be poorly populated (if at all). (Note that there are errors in § 4.1 of Klahn *et al.* (2021*b*), where coefficients 15 and 96, and similarly for subsequent calculations, should respectively be 6 and 24, in accordance with those above.)

To exemplify this, we will consider a single sample of the full data set utilized to create figure 9(*b*) ($k_ph = 1.2$, $\varepsilon = 0.1524$, $\mathcal{S} = 0.2688$), again generated utilizing the second-order irregular wave theory of Madsen & Fuhrman (2012). The sample considered contains n =24,050 randomly sampled surface elevations, corresponding to 0.01 % of the full data set generated for this case. The sample has skewness $\mathcal{S} = 0.2731$, with expected standard deviation $\sigma_{\mathcal{S}} = 0.0158$. The resulting p.d.f. created from the sampled data alone (using the same 0.2 bin size) is presented in figure 13 (circles, with error bars calculated as before). The theoretical p.d.f. from (2.31) utilizing the sample skewness is likewise presented as the full line, which is seen to closely resemble that from figure 9(*b*).

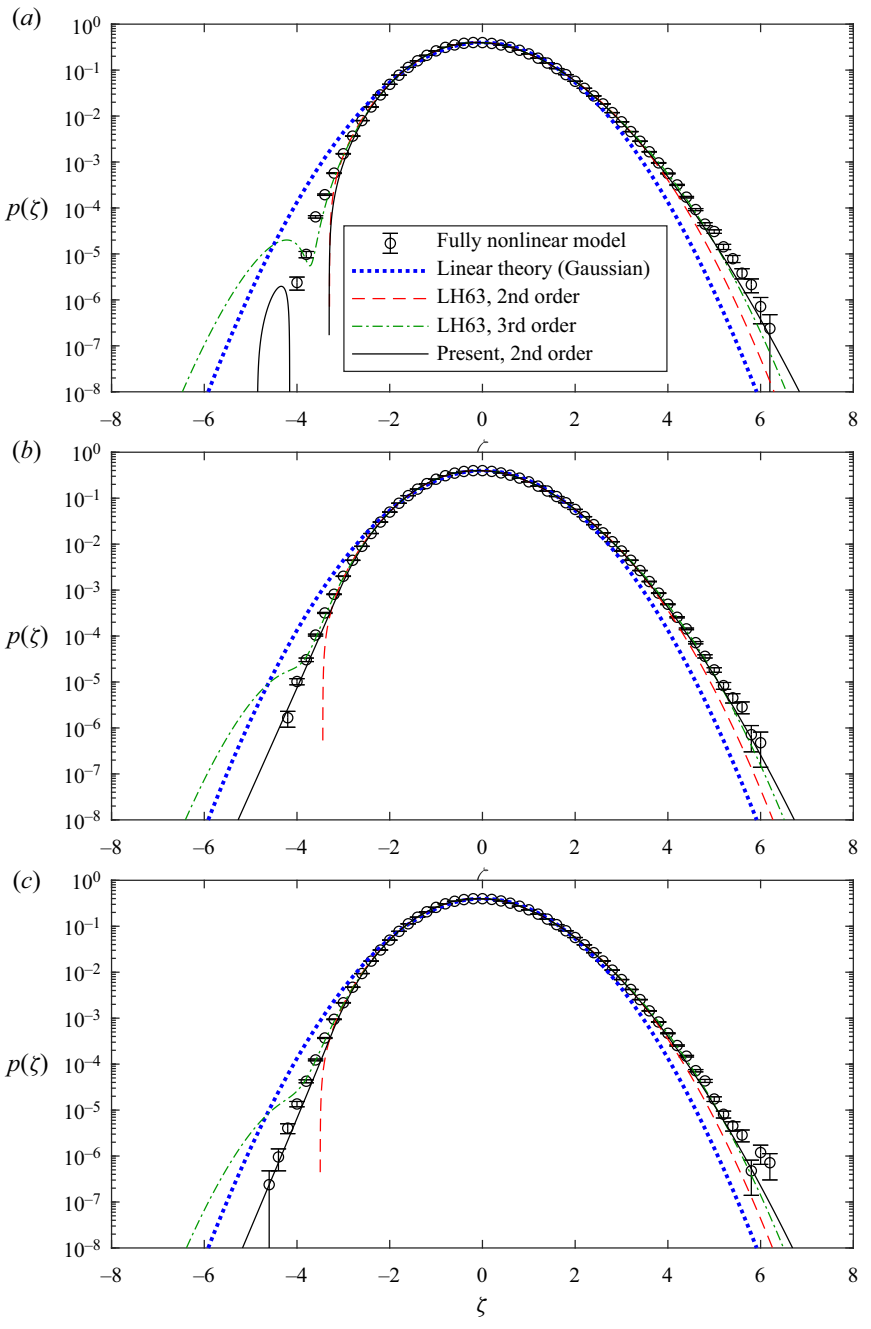

Figure 12. Comparison of the p.d.f.s from (*a*) (2.31) and (*b*,*c*) (5.3) (full lines) with those from data generated using the fully nonlinear model of Klahn *et al.* (2021*c*) (circles, with error bars). The Gaussian distribution (dotted lines) and those from LH63 (second order, dashed lines; third order, dashed-dotted lines) are also provided as a reference. Cases utilize $N_D = 2$ coupled with (*a*) $\varepsilon = 0.1048$, $k_p h = 1.0$; (*b*) $\varepsilon = 0.1270$, $k_p h = 1.5$; and (*c*) $\varepsilon = 0.1443$, $k_p h = \infty$, with other statistical quantities given in table 2. The legend applies to all panels.

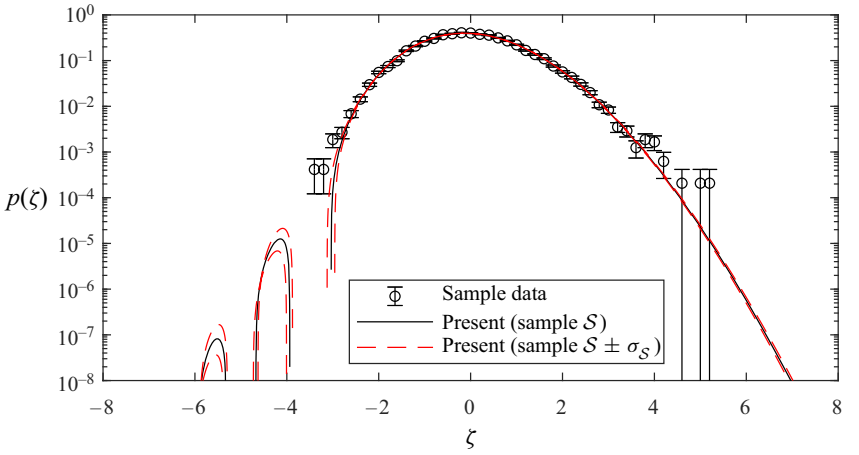

Figure 13. Comparison of p.d.f.s based on sample data generated from the second-order irregular wave theory of Madsen & Fuhrman (2012) (circles, with error bars), the new second-order p.d.f. (2.31) based on the sample skewness $\mathcal{S} = 0.2731$ (full line) and the p.d.f. using $\mathcal{S} \pm \sigma_{\mathcal{S}}$ (dashed lines), where $\sigma_{\mathcal{S}} = 0.0158$. The data utilized in this example (sample size $n = 24\,050$) correspond to a random sample of 0.01 % of the full data set used to create figure 9(*b*).

Additionally, the theoretical p.d.f.s from (2.31), now utilizing $\mathcal{S} \pm \sigma_{\mathcal{S}}$, are shown as the dashed lines, such that the (very thin) region between them can be taken as an indication of the uncertainty in the theoretical p.d.f. As suggested above, this uncertainty is very small relative to that associated with the sample p.d.f. (as indicated by the error bars), especially e.g. in the (poorly populated) positive tail. Indeed, the sample p.d.f. could hardly be utilized at all in this example to reliably predict the distribution for say $\zeta > 4$. Conversely, the uncertainty of the theoretical p.d.f. is small for the entire range shown, such that it may be reliably utilized to predict the theoretical probability of extreme surface elevations with say $\zeta > 6$. It is hoped that this example illustrates how the theoretical p.d.f. may be utilized in practice (including assessment of uncertainties), requiring only knowledge of the sample skewness and size.

8. Conclusions

In this work we have re-visited the derivation of the p.d.f. of the free surface elevation in an irregular sea, to second order in the wave steepness. To the order retained, we have derived exact results utilizing both moment and cumulant generating functions, and established their asymptotic equivalence in the limit of small skewness. The derivation of the p.d.f. stemming from the cumulant generating function has utilized a novel change in variables coupled with complex analysis, resulting in a new theoretical result, where the p.d.f. is expressed in terms of the Airy function, presented as (2.31) herein. Due to approximations made in his derivation, it is shown that the classical p.d.f. of Longuet-Higgins (1963) (referred to as LH63 herein), when truncated at second order, corresponds to that derived from the moment generating function, even though his derivation was based on the cumulant generating function. The new second-order p.d.f. predicts increased probability density of extreme positive surface elevations, typical of rogue waves, even relative to the third-order approximation of LH63. This heavy tail is inherent, and has been explained through comparison of the asymptotic forms of the p.d.f.s in the limit of large surface elevations. Similar to the p.d.f. of LH63, the new theoretical solution suffers from spurious

oscillations (and negative probability densities) for moderate to extreme negative surface elevations. A semi-theoretical means for remedying this shortcoming has been developed, based on inspection of the envelope of the Airy functions having negative arguments. This modified variant of the p.d.f. is presented as (5.3) herein, and maintains reasonable statistical moments provided that the skewness is less than or equal to 0.2. The new p.d.f.s have been compared against those from data sets involving storm conditions, generated from both second-order irregular wave theory as well as from simulations based on a fully nonlinear wave model. Good accuracy has been collectively demonstrated for the resulting p.d.f.s in both finite and infinite water depth, for varying degrees of directional spreading.

Supplementary material. Data utilized in the present study are freely available at https://doi.org/10.11583/DTU.21937232. The data set includes the surface elevation time series generated by the irregular wave theory of Madsen & Fuhrman (2012) considered in § 6.1, as well as the surface elevation maps generated by the fully nonlinear PFL model of Klahn *et al.* (2021*c*) considered in § 6.2. A Matlab function pdfAiry.m computing the new p.d.f. from (5.3) if $\mathcal{S} \leqslant 0.2$ and (2.31) otherwise is also provided. The PFL model is available as open source at https://github.com/MathiasKlahn/PFL-Wave-Model. Additionally, a Matlab implementation of the multi-directional irregular wave theory of Madsen & Fuhrman (2012), complete to third order, is freely available at https://doi.org/10.11583/DTU.22060124.

Acknowledgements. The second author gratefully acknowledges help from two anonymous contributors at the Mathematics Stack Exchange, in working out a form of the integral in § 2.2 (thread: https://math.stackexchange.com/q/4403218). The first author likewise acknowledges enlightening discussions with Professor M. Benoit, which resulted in important revisions to § 5.1.

Funding. This research has been financially supported by the Independent Research Fund Denmark project STORM: STatistics and fOrces on stRuctures from extreMe water waves in finite depth (D.R.F., grant ID: 10.46540/2035-00064B). This support is greatly appreciated.

Declaration of interests. The authors report no conflicts of interest.

Author ORCIDs.
David R. Fuhrman https://orcid.org/0000-0002-2433-6778;
Mathias Klahn https://orcid.org/0000-0003-0055-1489;
Yanyan Zhai https://orcid.org/0000-0001-6344-546X.

Appendix A. Corrigendum to the multi-directional irregular wave theory of Madsen & Fuhrman (2012)

As the multi-directional irregular wave theory of Madsen & Fuhrman (2012) has (to second order) been utilized in the present work (§ 6.1), we take the opportunity to correct some unfortunate errors that appeared in the original paper, which have recently come to light. Below, equation numbers referred to and notation are as in Madsen & Fuhrman (2012). Known corrections follow.

The second part of (3.11) should read

$$B_{2n} = \frac{1}{2}B_{n+n} = \frac{1}{h}a_n b_n. \tag{A1}$$

Equation (3.83) should read

$$\mu_{n\pm 2m} = \Pi[\{\omega_{1n}, \boldsymbol{k}_n\}, \{\pm\omega_{1m}, \pm\boldsymbol{k}_m\}, \{\pm\omega_{1m}, \pm\boldsymbol{k}_m\}, \{G_{n\pm m}, F_{n\pm m}\}, \{G_{n\pm m}, F_{n\pm m}\}, \{G_{2m}, \pm F_{2m}\}, \{F_{n\pm 2m}\}]. \tag{A2}$$

Finally, (3.84) should read

$$\mu_n^* = F_{13n}\cosh h\kappa_n + c_n^2 \Xi_{nn} + \sum_{\substack{m=1 \\ m\neq n}}^{N} c_m^2 \Xi_{nm}. \tag{A3}$$

The errors above were first pointed out through personal communication initiated by Professor M. Benoit, which Professor P.A. Madsen and the present first author gratefully acknowledge.

References

Abramowitz, M. & Stegun, I.A. 1964 *Handbook of Mathematical Functions with Formulas, Graphs, and Mathematical Tables*, 9th edn. Dover.

Battjes, J.A. 1974 Surf similarity. In *Proceedings of 14th Conference on Coastal Engineering, Copenhagen*, pp. 466–480. ASCE.

Berg, C. 2013 *Complex Analysis*. University of Copenhagen.

Fisher, R.A. 1930 The moments of the distribution for normal samples of measures of departure from normality. *Proc. R. Soc. Lond.* A **130**, 16–28.

Forristall, G.Z. 2000 Wave crest distributions: observations and second-order theory. *J. Phys. Oceanogr.* **30**, 1931–1943.

Fuhrman, D.R. & Bingham, H.B. 2004 Numerical solutions of fully non-linear and highly dispersive Boussinesq equations in two horizontal dimensions. *Intl J. Numer. Meth. Fluids* **44**, 231–255.

Hasselmann, K. *et al.* 1973 Measurements of wind-wave growth and swell decay during the Joint North Sea Wave Project (JONSWAP). Deutsches Hydrographisches Institut, Hamburg.

Karmpadakis, I., Swan, C. & Christou, M. 2020 Assessment of wave height distributions using an extensive field database. *Coast. Engng* **157**, 103630.

Klahn, M., Madsen, P.A. & Fuhrman, D.R. 2021*a* On the statistical properties of inertia and drag forces in nonlinear multi-directional irregular water waves. *J. Fluid Mech.* **916**, A59.

Klahn, M., Madsen, P.A. & Fuhrman, D.R. 2021*b* On the statistical properties of surface elevation, velocities and accelerations in multi-directional irregular water waves. *J. Fluid Mech.* **910**, A23.

Klahn, M., Madsen, P.A. & Fuhrman, D.R. 2021*c* Simulation of three-dimensional nonlinear water waves using a pseudospectral volumetric method with an artificial boundary condition. *Intl J. Numer. Meth. Fluids* **93**, 1843–1870.

Lawrence, C., Trulsen, K. & Gramstad, O. 2022 Extreme wave statistics of surface elevation and velocity field of gravity waves over a two-dimensional bathymetry. *J. Fluid Mech.* **939**, A41.

Liu, S., Zhang, X., Yang, J. & Yao, J. 2022 Modulational instability and statistical properties of irregular waves in finite water depth. *Appl. Ocean Res.* **120**, 103031.

Longuet-Higgins, M.S. 1952 On the statistical distribution of the heights of sea waves. *J. Mar. Res.* **11**, 245–266.

Longuet-Higgins, M.S. 1963 The effect of non-linearities on statistical distributions in the theory of sea waves. *J. Fluid Mech.* **17**, 459–480.

Madsen, P.A. & Fuhrman, D.R. 2012 Third-order theory for multi-directional irregular waves. *J. Fluid Mech.* **698**, 304–334.

Nicholls, D.P. 2011 Efficient enforcement of far-field boundary conditions in the transformed field expansions method. *J. Comput. Phys.* **230**, 8290–8303.

Onorato, M., *et al.* 2009 Statistical properties of mechanically generated surface gravity waves: a laboratory experiment in a three-dimensional wave basin. *J. Fluid Mech.* **627**, 235–257.

Socquet-Juglard, H., Dysthe, K., Trulsen, K., Krogstad, H.E. & Liu, J. 2005 Probability distributions of surface gravity waves during spectral changes. *J. Fluid Mech.* **542**, 195–216.

Song, J.-B. & Wu, Y.-H. 2000 Statistical distribution of water-particle velocity below the surface layer for finite water depth. *Coast. Engng* **40**, 1–19.

Tang, T. & Adcock, T.A.A. 2021 The influence of finite depth on the evolution of extreme wave statistics in numerical wave tanks. *Coast. Engng* **166**, 103870.

Tang, T., Barratt, D., Bingham, H.B., van den Bremer, T.S. & Adcock, T.A.A. 2022 The impact of removing the high-frequency spectral tail on rogue wave statistics. *J. Fluid Mech.* **953**, A9.

Tayfun, M.A. 1980 Narrow-band nonlinear sea waves. *J. Geophys. Res.* **85**, 1548–1552.

TAYFUN, M.A. & ALKHALIDI, M.A. 2020 Distribution of sea-surface elevations in intermediate and shallow water depths. *Coast. Engng* **157**, 103651.

TOFFOLI, A., BENOIT, M., ONORATO, M. & BITNER-GREGERSEN, E.M. 2009 The effect of third-order nonlinearity on statistical properties of random directional waves in finite depth. *Nonlinear Process. Geophys.* **16**, 131–139.

TOFFOLI, A., GRAMSTAD, O., TRULSEN, K., MONBALIU, J., BITNER-GREGERSEN, E. & ONORATO, M. 2010 Evolution of weakly nonlinear random directional waves: laboratory experiments and numerical simulations. *J. Fluid Mech.* **664**, 313–336.

XIAO, W., LIU, Y., WU, G. & YUE, D.K.P. 2013 Rogue wave occurrence and dynamics by direct simulations of nonlinear wave-field evolution. *J. Fluid Mech.* **720**, 357–392.

ZHANG, J. & BENOIT, M. 2021 Wave-bottom interaction and extreme wave statistics due to shoaling and de-shoaling of irregular long-crested wave trains over steep seabed changes. *J. Fluid Mech.* **912**, A28.